

Elucidating Carrier Dynamics and Interface Engineering in Sb₂S₃:
Toward Efficient Photoanode for Water Oxidation

Peer-reviewed author version

DEI TOS, Irene; Simbula, Angelica; Guerrero, Julian; Dong , Thanh; de la Fuente, Beatriz; SUBRAMANIAM, Sownder; Jose, Vishal K.; KUANG, Yinghuan; AERNOOTS, Tom; Naghavi, Negar; SHUKLA, Sudhanshu & VERMANG, Bart (2025) Elucidating Carrier Dynamics and Interface Engineering in Sb₂S₃: Toward Efficient Photoanode for Water Oxidation. In: ChemSusChem, 18 (14).

DOI: 10.1002/cssc.202402764

Handle: <http://hdl.handle.net/1942/46417>

Elucidating Carrier Dynamics and Interface Engineering in Sb₂S₃: Towards Efficient Photoanode for Water Oxidation

Irene Dei Tos,^{1,2,3†} Angelica Simbula,^{4†} Julian Guerrero,⁵ Thanh Dong,⁵ Sownder Subramaniam,^{1,2,3} Beatriz de la Fuente,⁶ Vishal K. Jose,^{1,2,3} Yinghuan Kuang,^{1,2,3} Tom Aernouts,^{1,2,3} Negar Naghavi,⁵ Sudhanshu Shukla,^{1,2,3*} Bart Vermang^{1,2,3}

¹Imec, Imo-imomec, Thor Park 8320, 3600 Genk, Belgium

²EnergyVille, Thor Park 8320, 3600 Genk, Belgium

³Hasselt University, Imo-imomec, Martelarenlaan 42, 3500 Hasselt, Belgium

⁴Dipartimento di Fisica, Università di Cagliari, 09042 Monserrato, Italy

⁵Institut Photovoltaïque d'Île-de-France (IPVF), UMR 9006, CNRS, Ecole Polytechnique - IP Paris, Chimie Paristech - PSL, 91120 Palaiseau, France

⁶Research Group Sustainable Materials Engineering (SUME), Lab of Electrochemical and SurfaceEngineering (SURF), Vrije Universiteit Brussel, Brussels1050, Belgium

† Equal contribution

*Corresponding author : sudhanshu.shukla@imec.be

Abstract

Conjugation of low-cost and high-performance semiconductors is essential in solar-driven photoelectrochemical (PEC) energy conversion. Sb_2S_3 is a wide-bandgap (≈ 1.7 eV) semiconductor with the potential to deliver a maximum photocurrent density of 24.5 mA cm^{-2} , making it highly attractive for PEC water splitting applications. However, bulk Sb_2S_3 exhibits intrinsic recombination issues and low electron-hole separation, posing a limit to photocurrent generation. This study clarifies the carrier dynamics by ultrafast spectroscopy measurements and proposes the design of a heterojunction between Sb_2S_3 and SnO_2 , with suitable band-edge energy offset. The $\text{SnO}_2/\text{Sb}_2\text{S}_3$ heterojunction enhances the charge separation efficiency, resulting in improvement of the photocurrent. The $\text{SnO}_2/\text{Sb}_2\text{S}_3$ photoanode, fabricated entirely by vapor deposition processes, demonstrated photoelectrochemical water oxidation with a photocurrent density up to ca. 3 mA cm^{-2} at 1.38 V vs RHE .

1. Introduction

As CO₂ generation's trend increases, a main challenge is contrasting it with renewable energy resources *via* production of clean and inexpensive energy.^[1,2] Among the various energy approaches to generate renewable fuels, solar-driven photo-electrochemical (PEC) water splitting provides a promising path to produce sustainable fuel in the form of H₂.^[3] A typical PEC water splitting system comprises of semiconducting photoelectrodes combined with proper cocatalysts to perform oxidation evolution reaction (OER) (at photoanode) and hydrogen evolution reduction reactions (HER) (at photocathode).^[4] The overall PEC-water splitting reaction envisages three major steps: (i) absorption of light by a semiconductor (also indicated as absorber) and generation of electron-hole pairs; (ii) electron-hole separation and carriers' migration to the surface of semiconductor; (iii) surface reactions for water reduction or oxidation.^[5] To perform PEC reactions a photovoltage is required. The photovoltage can be achieved using a single material with an optimal bandgap, in which the conduction and valence band edges straddle the water redox potentials (1.23 V vs. NHE).^[6]

For practical realization of PEC devices, reports suggest that the photoactive material must meet some specific requirements: efficient absorption with wide coverage of the solar spectrum, high corrosion resistance in aqueous electrolyte solutions, high solar-to-hydrogen (STH) conversion efficiency over 10%, cost effective by using abundant materials and toxic-free materials and easy deposition processes.^[7] As a result, the scientific community is actively exploring low-cost, abundant, and non-toxic semiconductors with excellent optoelectronic properties to support PEC applications on a scale that meets global energy demands.

Antimony sulfide (Sb₂S₃) has emerged as a promising earth-abundant semiconductor material.^[8] Its low melting point ($\approx 500^\circ\text{C}$) and high vapor pressures facilitate easy and low-temperature thin film fabrication.^[9] Additionally, Sb₂S₃ is a binary compound with a single stable phase, which eliminates the risk of forming undesirable secondary phases during synthesis.^[10] Furthermore the bandgap (E_g , 1.7 eV) and a high absorption coefficient (α) of striking 10^5 cm^{-1} , make it a nearly ideal semiconductor material for PEC.^[11] Theoretically, Sb₂S₃ is estimated to deliver a maximum photocurrent density of approximately 24.5 mA cm^{-2} under simulated solar irradiation (AM 1.5 G).^[12] However, the intrinsic bulk defects, such as sulfur vacancies (V_s) and antisite (S_b) defects, lead to energy states/band deep in the energy gap causing carrier recombination and undesirable photocarrier losses.^[13,14] Moreover, the development of Sb₂S₃-based photoanodes is also limited by poor electron-hole separation.^[15]

Recombination and carrier separation in polycrystalline thin film absorbers critically relates with the quality of the absorber layer. Typically, Sb_2S_3 thin films are fabricated *via* solution^[16] or vacuum processes.^[17,18] The most explored solution processes include chemical bath deposition,^[19] spray pyrolysis,^[20] and hydrothermal deposition.^[21] While offering facile advantages, chemical bath deposition and hydrothermal deposition are time-consuming processes, and they pose stringent requirements on the substrate as well as on device scalability.^[22] Spray pyrolysis, while accelerating deposition time and overcoming the scalability issue, cannot allow precise control of oxygen content, making it difficult to prevent the formation of antimony oxide during the Sb_2S_3 deposition.^[23]

The more conventional vacuum-based approach is thermal evaporation, which is known for ensuring the formation of compact and uniform thin films with high throughput.^[24] To mitigate the formation of V_s , a post-deposition sulfurization step necessary to promote solid-state crystallization helps inhibit oxide formation, enabling the growth of large grain sulfur-rich thin films.^[25] This strategy helps in reducing V_s and Sb_s formation, ultimately improving electron-hole separation.^[26]

Heterojunction engineering between two semiconductors is a practical methodology to circumvent low electron–hole separation.^[27–29] The formation of a heterojunction allows for the creation of a built-in electric field, overcoming the poor charge separation efficiency and improving the photocurrent.^[30] To form an effective heterojunction, two semiconductors are involved, which must have properly aligned band structures.^[31] Heterojunction engineering to suppress recombination in Sb_2S_3 absorber has been extensively explored, with a variety of oxide semiconductors used in combination with Sb_2S_3 , such as TiO_2 ,^[32] Al_2O_3 ,^[33,34] ZnO ^[35, 36] and SnO_2 .^[37,38]

SnO_2 is an ideal inorganic electron extraction material, extensively investigated in the field of methylammonium lead iodide (MAPbI_3)-based perovskites (PSC) as electron transport layer (ETL).^[39–41] The choice of SnO_2 (3.6–4.1 eV) as ETL in a photoanode configuration for OER, owns numerous advantages: i) lower conduction band states that accelerates the electron injection; ii) high electron mobility for enhancing the electron extraction and transport, decreasing the carrier recombination; iii) low crystallization temperature with reduced fabrication cost; iv) excellent lattice match with conductive glasses as FTO or ITO.^[42]

In this study, we demonstrate the formation of a heterojunction between a thermally evaporated S-rich Sb_2S_3 and sputtered SnO_2 thin film. Thanks to its well-matched band alignment with Sb_2S_3 as well as a higher electron mobility ($> 400 \text{ cm}^2 \text{ V}^{-1} \text{ s}^{-1}$),^[43] SnO_2 will facilitate electron charge transportation in the photoanode. We further applied a thin layer ($\sim 5 \text{ nm}$) of NiO_x as

hole transport layer (HTL) in an attempt to further improve hole transfer and stability, finalizing the device configuration.^[44,45] The study envisages the usage of newly developed strategies for the low temperature soft sputtering of SnO₂ and NiO_x, which description will be detailed elsewhere.

The choice of the evaporation route for the deposition of the CTLs, Sb₂S₃ and metal contact, proves an advantage for scalability, and it is motivated by the high versatility of this process and the easy assembly of the photoanode. The choice of the SnO₂ as ETL and NiO_x as HTL was inspired by the recent successes obtained for methylammonium lead iodide (MAPbI₃)-based perovskites (PSC),^[43] which shares a similar bandgap of ~ 1.7 eV with Sb₂S₃. The proper band alignment with Sb₂S₃ absorber and the large optical bandgap of SnO₂ and NiO_x are successful features that enable the achievement of a photocurrent density (J) for OER of ~3 mA cm⁻² at 1.38 V vs RHE. To date, the highest photocurrent density achieved is of approximately 4.21 mA cm⁻² at 1.23 V vs RHE for a ternary TiO₂/BiNP/Sb₂S₃ photoanode, with an Applied Bias Photon-to-current Efficiency (ABPE) of 1.56%.^[46]

2. Results and Discussion

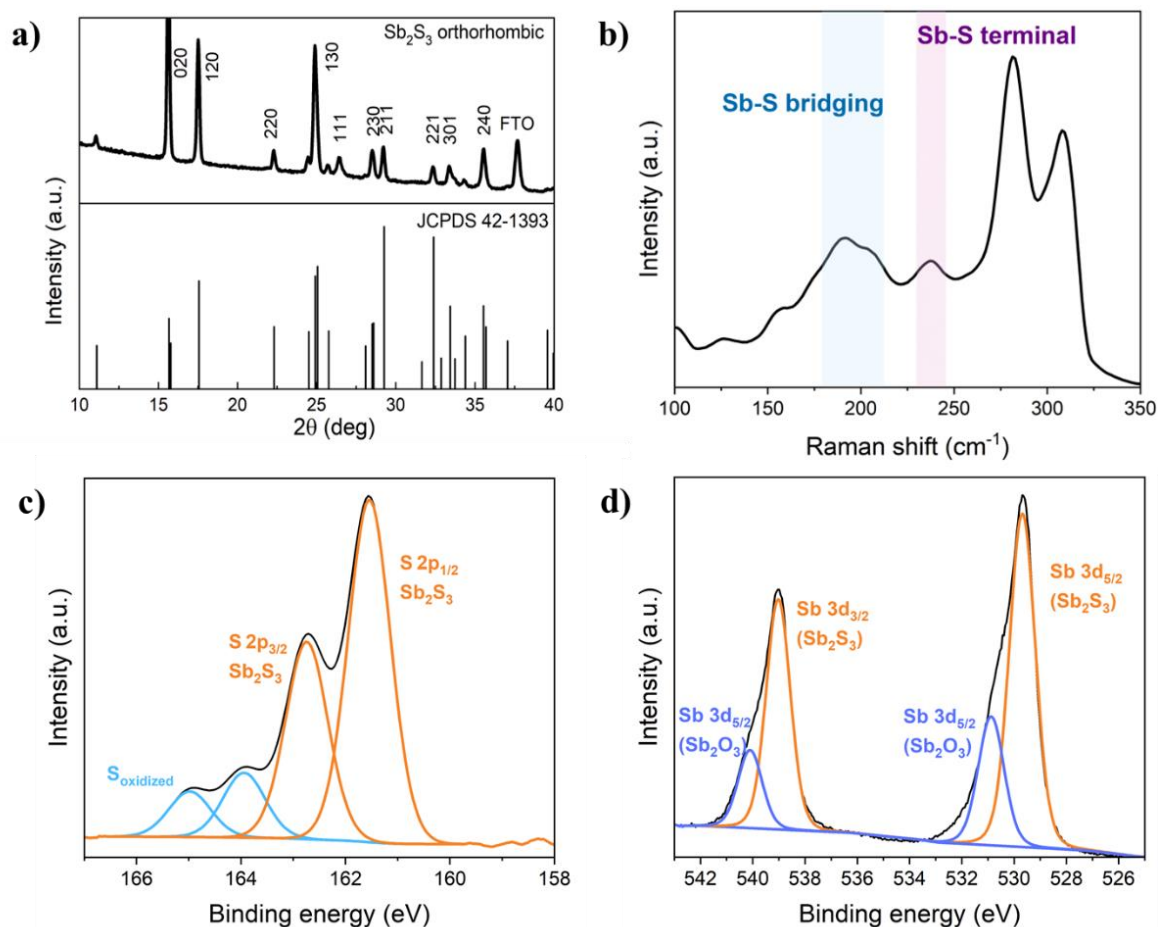


Figure 1. a) XRD patterns, b) Raman spectra, and c) S 2p d) Sb 3d XPS high resolution spectra of Sb₂S₃ thin films prepared by thermal evaporation on FTO coated glass.

The S-rich Sb₂S₃ thin films were deposited on fluorine tin oxide (FTO) coated glass and then characterized by X-ray diffraction (XRD) analysis to identify the crystallographic information of the absorber, as shown in **Fig. 1a**. XRD data showed characteristic reflections of (020), (120), (130), (240) (called $(hk0)$) planes, and (111), (211), (221) (called (hkl)) planes. The peaks were consistent with orthorhombic Sb₂S₃ phase with a space group of $Pbnm$ (JCPDS No. 42-1393, $Pbnm$).^[47] This is indicative of a phase-pure formation without any secondary phases or impurities. Sb₂S₃ possesses a *quasi*-1D crystal structure consisting of [Sb₄S₆]_n units bonded covalently together in the *c*-axis direction to form [Sb₄S₆]_n ribbons.^[16] The (hkl) reflections of Sb₂S₃ are attributed to the longitudinal direction of the ribbons (i.e., [001] direction) oriented perpendicular to the substrate, while $(hk0)$ identifies the direction orthogonal to the substrate. The Sb₂S₃ revealed large peak intensities relative to the $(hk0)$ planes, while low peak intensities

were detected for the (*hkl*) planes. The presence of both the (*hkl*) and (*hk0*) planes in Sb₂S₃ XRD patterns revealed that Sb₂S₃ has a randomly oriented grain structure with various facets. [48]

Furthermore, the Raman spectrum of the deposited layers (**Fig. 1b**) can be assigned to the Sb₂S₃ phase. Seven Raman bands are detected and can be attributed to: the asymmetric and symmetric bending vibration of S–Sb–S at 189 and 237 cm⁻¹; the asymmetric and symmetric stretching vibration of Sb–S appear at 282 and 309 cm⁻¹ respectively; the crystalline Sb₂S₃ phase at 126 and 152 cm⁻¹. [49] The peak located at 189 cm⁻¹ was assigned to Sb–S bridging vibrations and corresponds to internal Sb–S bonding within the Sb–S polymeric chain (rather than the edge states of the Sb–S chain). On the other side, the peak at 237 cm⁻¹ was attributed to Sb–S terminal vibrations resulting from either Sb–S bonding of the edge states in the Sb–S chain or simple Sb–S bonds without forming an Sb–S chain. [50]

Moreover, X-ray photoelectron spectroscopy (XPS) analyses were conducted to examine the surface chemical compositions and oxidation states of the Sb₂S₃ thin films. XPS spectrum of Sb 3d (**Fig. 1d**) displays two peaks located at 538.2 and 528.9 eV that were attributed to Sb_{3/2} and Sb_{5/2} of the Sb₂S₃ phase, respectively. In addition, the two peaks near 540 and 532.5 eV were assigned to Sb_{3/2} and Sb_{5/2} of the native antimonious oxide (α -Sb₂O₃) phase. The α -Sb₂O₃, usually arises as an oxide impurity during the synthesis and can be mostly ascribed to long-term air exposure oxidation of the sample before XPS testing. [51] The presence of α -Sb₂O₃ in principle does not alter the thin film properties, rather, it has the potential to function as a passivation layer, thereby stabilizing the film when exposed to the atmosphere. The high-resolution S 2p spectrum revealed two peaks at 162.5 and 161.0 eV (**Fig. 1c**) that were ascribed to the oxidation states of S²⁻ in Sb₂S₃. [51] XRD, Raman, and XPS analysis together confirm the presence of the single orthorhombic phase of Sb₂S₃, without any formation of secondary phases nor relevant additional impurities.

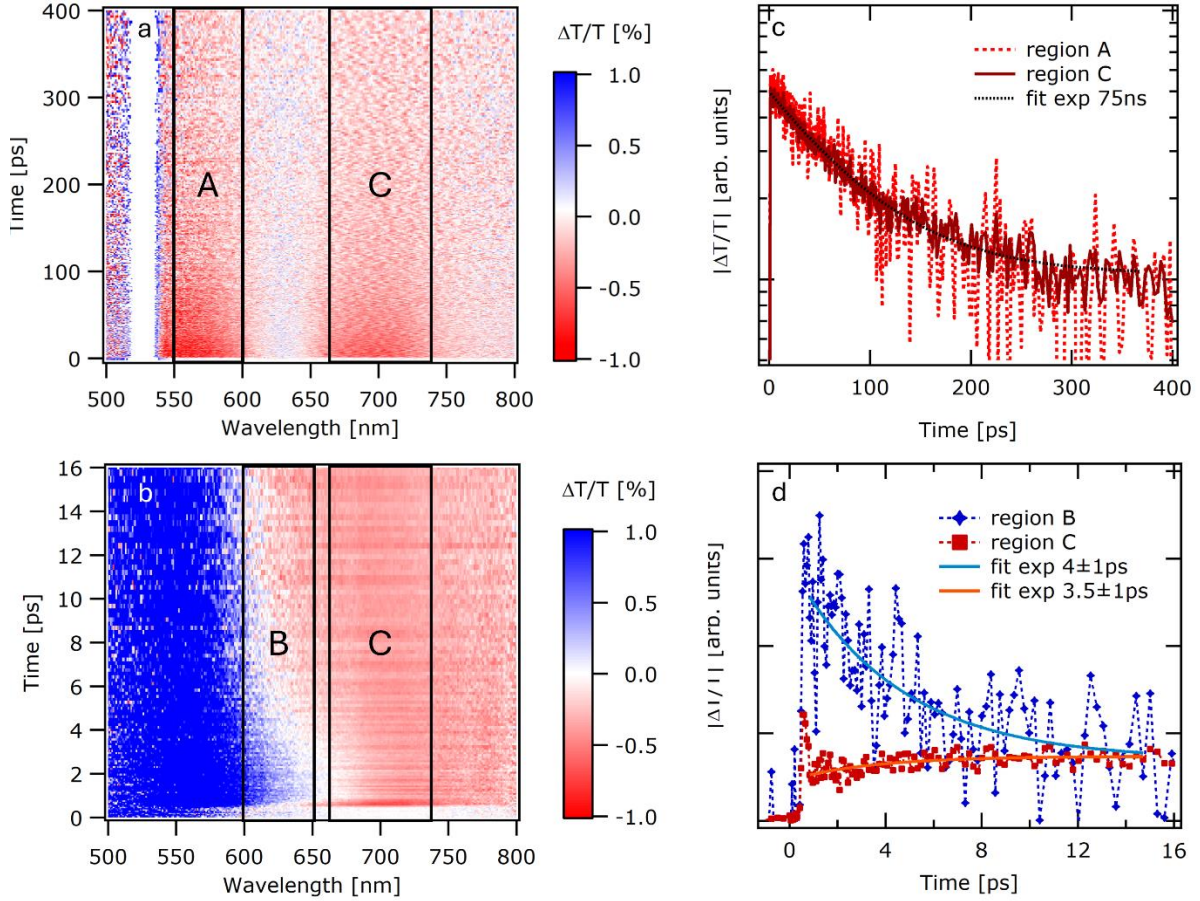


Figure 2. Time-resolved Differential Transmission ($\Delta T/T$) spectrograms in **a)** long and **b)** short time range for Sb_2S_3 deposited on FTO, with subtraction of background noise at negative time delays. Red color (negative $\Delta T/T$) indicates the photoinduced absorption and blue color (positive $\Delta T/T$) stands for photobleaching signal. Three wavelength regions were identified as A (550-600nm), B (600-650nm) and C (650-750nm). Time decays of $|\Delta T/T|$ extracted from spectrograms **a)** and **b)** respectively, with the absolute value of photoinduced signal (negative $\Delta T/T$) in region A and C are reported in **c)** as dashed and solid red lines, respectively. Panel **d)** compares the absolute value of photoinduced absorption in region C (red squares) with the photobleaching of region B (blue diamonds). Time traces are fitted with mono-exponential functions resulting in a 75-ns decay for the long-time component, and a picosecond timescale rise and fall for the photoinduced and photobleaching signals respectively.

The optoelectronic properties of Sb_2S_3 thin films were analyzed by means of UV-Vis optical absorption spectroscopy. From the absorption plot (**Fig.S1**), a strong absorption onset at ~ 700 nm can be detected. The band gap energy can be determined through linear extrapolation using a Tauc plot, from which $E_g \sim 1.65$ eV was obtained for assuming direct transition ($n = 2$ in the Tauc relation). The optical band gap falls within the range of reported experimental values for Sb_2S_3 .^[52]

Ultrafast spectroscopy measurements were conducted by means of transient differential transmission measured in a pump and probe configuration to check the stoichiometry of the semiconductor and to explore charge formation and trapping processes. The sample Sb_2S_3 was excited with a pump laser at 530 nm and probed with transmitted white pulses in two different configurations (see Methods section), with results reported in **Fig. 2**. Measurement with longer time delay (400ns) allows to identify two broad photoinduced features A and C, as shown in the spectrogram (**Fig. 2a**). Study from Lian *et al.* shows a clear distinction between Sb-rich and S-rich absorber,^[53] as the optoelectronic quality of the absorber is critically governed by stoichiometric factors with S-rich being favourable owing to lesser defects. For Sb-rich Sb_2S_3 , a photoinduced absorption (PIA) signal is expected to arise only in region A, whereas S-rich condition features an additional component in region C. The result of our measurements clearly indicate that the produced Sb_2S_3 absorbers were S-rich in nature, which is desirable for application of these films in optoelectronic devices. S-rich behaviour is expected as the films were subjected to post-sulfurization treatment. This highlights the importance of appropriate annealing conditions for preparing Sb_2S_3 thin films. Upon further analysis of photo transients, long-living photoinduced absorption from trapped carriers is visible from the time decays extracted from regions A and C as shown in **Fig. 2c**. A lifetime of 75 ns was obtained by fitting the decay with a mono-exponential function, compatible with the previous data observed for this material.^[54]

Measurements conducted with shorter time delay and higher resolution resulted in spectrogram shown in **Fig. 2b**: an ultrafast photobleaching (PB) spectral feature appears in wavelength range B, that was not visible in the long-range measurement. The transfer between the photobleaching signal B and the photoinduced absorption C is showing a charge trapping mechanism occurring over a time of few picoseconds, as highlighted also by time decays shown in **Fig. 2d**. This behaviour can be associated with self-trapped excitons (STEs) formation and is compatible with previous observation from Yang *et al.*^[55] STEs formation is an intrinsic mechanism responsible for carrier trapping and clamping of the maximum achievable photovoltages. Based on above analysis, a schematic of the photophysical process, where the formation of STE proceeds via a one- or two- steps process, is shown in **Fig. 3**.

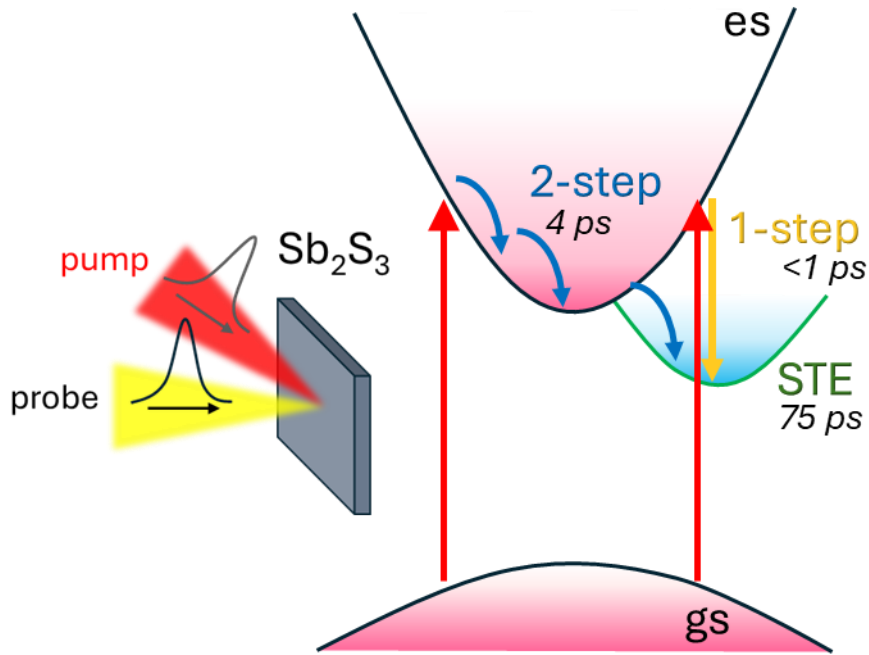


Figure 3. Representative schematic of the photophysical processes involved in Sb_2S_3 film based on ultrafast pump probe spectroscopy measurements, sketching the transitions between ground state (gs) and excited state (es). Red arrows represent electrons excited from gs to es. The filling of self-trapped exciton (STE) state from excited state follows to possible decays, represented by yellow arrow (1-step process, sub-ps timescale) or blue arrows (2-steps process, 4 ps timescale).

The first process, represented by the blue arrows in **Fig. 3**, is the 2-step one, where hot electrons relax down to the STE state, which is attributed to the drop in the bleaching in band B within a few picoseconds, simultaneously with the charging of photoinduced signal in band C, on the same timescale, reported in **Fig. 2d**. The lifetime of the trapped exciton state estimated from the result of the fit on the photoinduced absorption signal with a monoexponential decay, is 75 ps. The initial spike in the photoinduced signal in spectral region C of **Fig. 2d** can be interpreted as a second possible process, which is the direct and ultrafast formation of the STE, represented by the yellow arrow in the sketch in **Fig. 3**. Although the explanation might sound speculative, the power dependence of the amplitude of the initial spike was verified to be the same as that of the photoinduced signal at longer time delays (**Fig. S2**), indicating that they are resulting from the same excitation species in the material. It can be also excluded that the ultrafast feature was due to nonlinear interactions with the substrates by comparison with reference measurements on substrates (**Fig. S3**). While the growth conditions to prepare Sb_2S_3 films in this study were kept fixed, it is to be noted that the defects responsible for the characteristic

signature in charge carrier dynamics are critically governed by the growth conditions. For instance, annealing in sulfur-rich conditions will likely create Sb vacancies (V_{Sb}) and/or antisite (Sb_S) defects and S-vacancies (V_S) and/or antisite S_{Sb} defects in S-poor conditions. Similarly, changes in annealing temperature can alter the defect density and their energetic position in the bandgap in a complex manner, leading to change in carrier dynamics. A more focused investigation on growth dependent carrier dynamics is currently on-going.

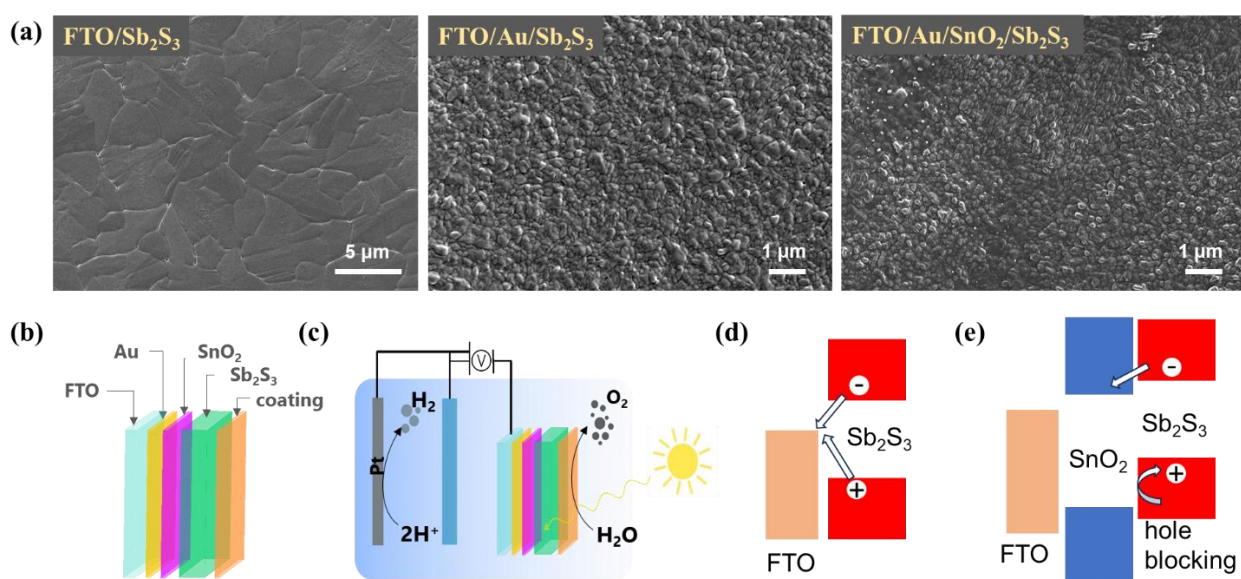


Figure 4. **a)** Surface SEM images of thermally evaporated Sb₂S₃ on different substrates **b)** Schematics of photoanode architecture **c)** Schematics of device working principles for PEC water oxidation. Schematics of activity of the Sb₂S₃-based photoanode **d)** without and **e)** with SnO₂ as ETL and holes block layer.

The morphology of the resulting Sb₂S₃ thin film was examined using scanning electron microscopy (SEM) analysis. The SEM images presented in **Fig. 4a** indicate that Sb₂S₃ absorber fabricated on FTO substrate is composed of planar and closely packed grains. To the best of our knowledge, this is among the largest grain size reported in literature for this semiconductor deposited on a conductive glass, where the average grain size is 2.5-5.0 μm based on evaporation deposition^[56] and ≈10 μm in case of hydrothermal deposition performed with lanthanides as dopants.^[57] Cross-sectional SEM analysis (**Fig. S4**) reveals that the Sb₂S₃ thin film is compact and conformal to the underlying substrate with non-visible GBs, which leads to the hypothesis of near monolithic grains. The thickness of the thin films, extrapolated from cross-section SEM images, is uniform and roughly 500 nm. The features of the Sb₂S₃ thin films

however are not retained when moving from FTO to Au or SnO₂ (**Fig. 4a**), indicating that the morphology of the thin films is strongly related to the underlying contact layer. The characterization on these three substrates led to conclude that phase pure Sb₂S₃ films prepared via thermal evaporation generates reproducible, S-rich thin films with a conformal and thickness coating to the substrate, which render the films desirable for device development.

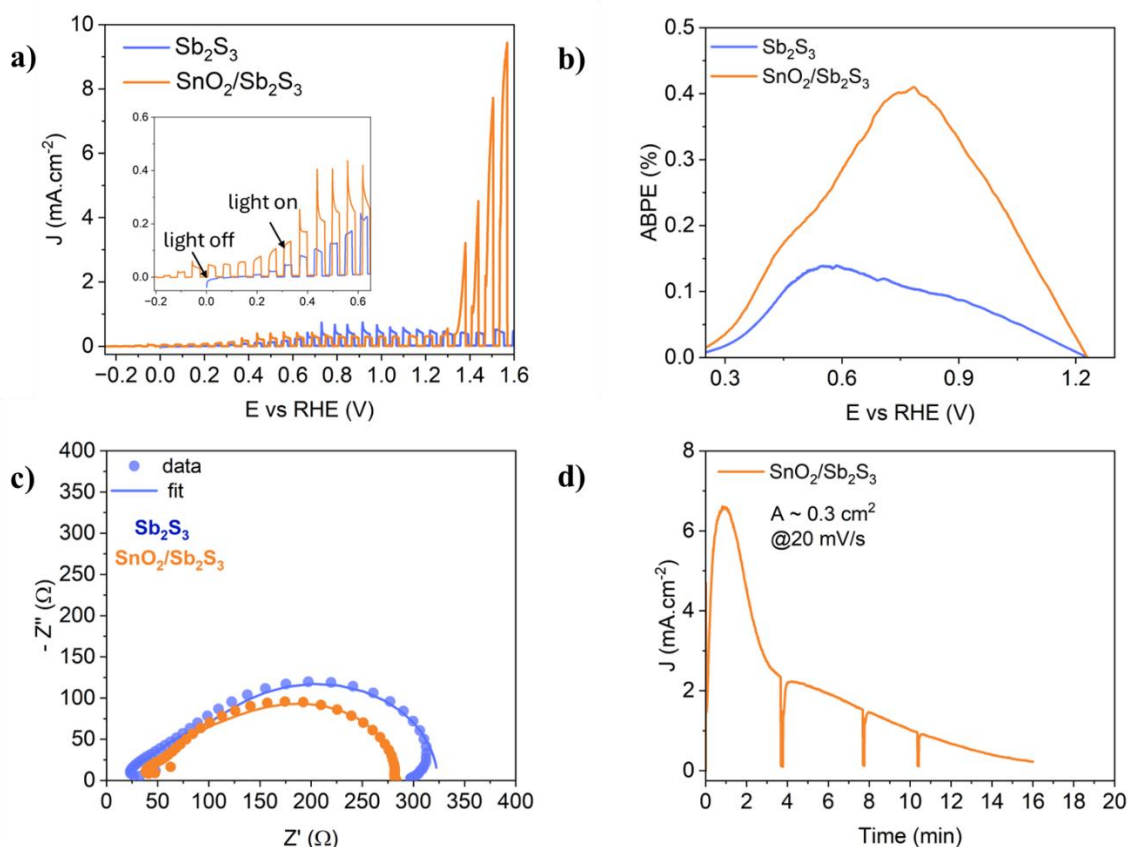


Figure 5. **a)** LSV scans of Sb₂S₃ and SnO₂/Sb₂S₃ electrodes for OER registered in 0.5 M Na₂SO₄ (pH 5) solution under 1 sun illumination (100 mW cm⁻²). Scan rate 10 mV/s. Electrode geometric surface area ~0.3 cm². **b)** Measured Applied Bias Photon-to-current Efficiency for Sb₂S₃ and SnO₂/Sb₂S₃ photoanodes. **c)** Nyquist plot of Sb₂S₃-photoanode with and without introduction of SnO₂ ETL under 1 Sun illumination **d)** Chronoamperometry of a SnO₂/Sb₂S₃ photoanode for OER in Na₂SO₄ (pH 5) solution at 1.35 V vs RHE.

PEC performances of the Sb₂S₃-based photoanode with and without SnO₂ ETL (**Fig. 4b**), were evaluated for OER. The device without any CTL, i.e. FTO/Au/Sb₂S₃ used as a reference sample for comparison. A thin Au layer in the stack acts as a tunnel junction between the FTO and Sb₂S₃, with the function of promoting the extractions of electrons towards the FTO back contact (**Fig. 4c**). Generally, the Au is usually used as back contact for a photoanode device owing to

its high work function. However, the thickness of the Au layer used in this study was sufficiently thin (10 nm) to allow tunneling of electrons. First, insights into the PEC performances of the Sb_2S_3 – based photoanodes were collected in 0.5 M Na_2SO_4 (pH 5) solution by LSV scans under intermittent simulated 1 sun illumination (100 mW cm^{-2}), comparing FTO/Au/ Sb_2S_3 and FTO/Au/ SnO_2 / Sb_2S_3 electrodes (**Fig. 5a**). By introducing the SnO_2 ETL a six-fold increase of the catalytic photocurrent from ~ 0.5 to 3 mA/cm^{-2} is observed, at about 1.38 V vs. RHE compared with the FTO/Au/ Sb_2S_3 electrode (**Fig. S5**). The enhancement of the photocurrent can be attributed to the presence of SnO_2 that promotes the electrons' extraction towards the contact, rendering more holes available for the reaction at the surface of the photoanode (**Fig. 4d, e**). It thereby confirms the presence of the ultrathin SnO_2 layer, though difficult to detect by SEM, EDX, and XRD analysis. Notably, the low-temperature annealing ($\sim 300 \text{ }^\circ\text{C}$) did not degrade the SnO_2 layer, allowing for an enhancement of the photocurrent with respect to the pristine device. It can be hypothesized that a junction is formed between the SnO_2 and Sb_2S_3 , which is responsible for the increase in the photocurrent of the device. Not only did the photocurrent improve with the introduction of SnO_2 in the photoanode, but the onset potential shifts from $\sim 0.45 \text{ V}$ to 0.2 V vs RHE (inset **Fig. 5a**).

We have studied the impact of the introduction of a thin NiO_x layer (5 nm) into the device as top layer. The addition of the NiO_x does not show an improvement of the photocurrent obtained. The reason for this can be manifold, the most trusted being that the NiO_x stability can be affected by the acidic conditions of the electrolyte. Besides, the addition of NiO_x can add electric resistance, explaining the smaller photocurrent generated (**Fig. S6**). Moreover, the drop in photocurrent at pH 5 can be explained by assuming that NiO_x operates only in near-neutral conditions by hindering the generation of photocurrent. This observation together with NiO_x instability at operational pH values, brings to its exclusion from the photoanode configuration.

The trend of photocurrent generated from Sb_2S_3 -based devices, is reproducible across different electrolytes and pH levels (**Fig. S7**). This trend exhibits intriguing characteristics and has been previously reported in the literature.^[42] The formation of a plateau between approximately 0.5 and 1.35 V vs. RHE can be explained by the excited state dynamics described above. From this perspective, the self-charge-trapping mechanism occurring within Sb_2S_3 grains, which is responsible for the generation of photoinduced signals, is likely the cause of the photocurrent clamping. Given the intrinsic nature of this phenomenon, doping the material with positive ions may be an effective strategy to prevent the formation of STEs, thereby enhancing both photovoltage and photocurrent generation.

The ABPE versus applied biases is presented in **Fig. 5b**. The maximum ABPE of the SnO₂/Sb₂S₃-based photoanode can reach 0.4% at ~ 0.8 V vs RHE, surpassing the one of the Sb₂S₃-based photoanode with a 4-fold increase. This furthermore confirms the positive role played by SnO₂ within the device.

Electrochemical impedance spectroscopy (EIS) under different light and bias conditions, was performed to understand the charge-transport process in the Sb₂S₃ photoanode with the addition of SnO₂ ETL. The resultant Nyquist plot is presented in **Fig. 5c**, and its equivalent circuit model is presented in **Fig. S8**. Here, the R_s mainly represents the sheet resistance of the contact, while R_p can be taken as the resistance between photoanode and electrolyte. The SnO₂/Sb₂S₃ photoanode exhibits a smaller R_p value of ~19.8 Ω (**Table 1**) when compared to the Sb₂S₃ photoanode without ETL (~34.5 Ω), measured at 1.35 V vs RHE under illumination. This confirms that the improvement in the *J* is provided by the introduction of the SnO₂ layer, that enhances the charge-transfer ability at the interface with the photoanode.

To evaluate the stability of the SnO₂/Sb₂S₃ photoanode, chronoamperometry (CA) tests under applied bias and light were performed, as shown in **Fig. 5d**. Long-term stability is a critical challenge for sulfide-based photoelectrodes towards solar driven OER, as metal sulfides are known to undergo photo corrosion during the photocatalysis process. In the case of Sb₂S₃, it can be inferred that sulfide ions (S²⁻) are likely to be oxidized by accumulated holes; this is accompanied by leaching of the free antimony ions (Sb³⁺). The SnO₂/Sb₂S₃ photoanode exhibits bare Sb₂S₃ on the surface, which leads to a photocurrent decrease within 15 minutes under illumination at applied bias of 1.35 V vs RHE. This highlights the need for future optimization of the photoanode surface exposed to the electrolyte, potentially through a protective coating. Although NiO_x does not enhance the photoanode's performance, it appears to be a promising candidate for improving device stability. However, the instability of NiO_x in acidic media, as evidenced in its Pourbaix diagram, poses a challenge in acidic PEC operation. This was confirmed by CA tests under applied bias and light: while NiO_x slightly extended the device's lifetime, it did not survive in the acidic environment, ultimately exposing the absorber to degradation (**Fig. S9**).

3. Conclusion

In this work we addressed the Sb₂S₃'s low electron-hole separation from several points of view. By optimization of the thermal evaporation process, we realize Sb₂S₃ thin films on FTO with large grains and low-density GBs, with morphological properties comparable to the best thin

films obtained by hydrothermal deposition. X-ray diffraction, X-Ray spectroscopy and Raman analysis confirmed the formation of phase-pure thin films. Subsequently, ultrafast spectroscopy measurements were used to explore charge formation and trapping processes in the as-deposited thin films. The analysis revealed the formation of S-rich Sb_2S_3 thin films and evidenced the presence of self-trapped excitons (STEs), an intrinsic mechanism responsible for carrier trapping. As outcome of differential transmission measurements, a twofold mechanism for STEs formation in Sb_2S_3 has been proposed, that can consist either of a 2-step process where hot electrons relax down to the STE state or, alternatively, the direct formation of the STE. The lifetime of the trapped exciton state has been estimated to be 75 ps.

The STEs mechanism predict the clamping of the maximum achievable photocurrent. Lastly, we used interface engineering to provide a mechanism that circumvents the low electron-hole separation. The Sb_2S_3 -based photoanode for OER was realized entirely by evaporation processes of the absorber, CTLs and metal contact, and optimized upon introduction of SnO_2 as ETL. Due to favorable band alignment between SnO_2 and Sb_2S_3 and the creation of a heterojunction at their interface, the FTO/Au/ SnO_2 / Sb_2S_3 photoanode can promote charge separation, resulting in an increase in the photocurrent density with respect to pristine device (FTO/Au/ Sb_2S_3). The resultant photoanode can deliver a J of $\sim 3 \text{ mA/cm}^2$ at the potentials of 1.38 V vs RHE, with an onset potential of -0.2 V vs RHE. The J generated in the potential window ~ 0.5 -1.35 V vs RHE is likely hindered by the formation of STEs and can find its explanation in the excited state dynamics, as stated above.

While further optimization for the durability of the device in liquid electrolyte is needed, this study indicates that we succeed in the interface engineering optimization. This is further confirmed by the measured ABPE and Nyquist impedance characterization.

Acknowledgements

S.S. acknowledge European Union's Horizon Europe program for funding under the Marie Skłodowska-Curie Grant Agreement No. 101067667. S.S. and B.V. acknowledge Catalisti VLAIO (Vlaanderen Agentschap Innoveren & Ondernemen) through the Moonshot SYN-CAT project (HBC.2020.2614), KESPER (M-ERA.NET) and Interreg FOTON project. S.S., B.V., and V.K.S. acknowledge support from Belgian federal government through the Energy Transition Fund for T-REX project. A.S. acknowledges CeSAR (Centro Servizi Ateneo per la Ricerca) at University of Cagliari and Dr. Marco Marceddu for technical assistance. A.S. was supported by PON R&I 2014-2020 CCI2014IT16M2OP005 Azione IV.4. Green - CUP

F35F21002390008. I.D.T. thanks FWO for the funding through the Fundamental Research PhD Fellowship (11PNM24N) and Travel Grant for a short stay abroad (V434524N).

Keywords

Carrier dynamics, photoelectrochemical cells, water splitting, charge transfer, heterojunction.

References

- [1] Z. Zhang, Y. Zheng, L. Qian, D. Luo, H. Dou, G. Wen, A. Yu, Z. Chen, Z. Zhang, Y. Zheng, L. Qian, D. Luo, H. Dou, G. Wen, A. Yu, Z. Chen, *Adv. Mater.* **2022**, *34*, 2201547.
- [2] J. Li, J. Ren, S. Li, G. Li, M. M. J. Li, R. Li, Y. S. Kang, X. Zou, Y. Luo, B. Liu, Y. Zhao, *Green Energy Environ.* **2024**, *9*, 859–876.
- [3] X. Zhang, Z. Li, L. R. Sinaga, M. Schwarze, R. Schomäcker, R. van de Krol, F. F. Abdi, *ACS Sustain. Chem. Eng.* **2024**, *12*, 13783–13797.
- [4] J. Yang, D. Wang, H. Han, C. Li, *Acc. Chem. Res.* **2013**, *46*, 1900-1909.
- [5] D. Reis Santos, S. Shukla, B. Vermang, *J. Mater. Chem. A* **2023**, *11*, 22087-22104
- [6] M. G. Walter, E. L. Warren, J. R. Mckone, S. W. Boettcher, Q. Mi, E. A. Santori, N. S. Lewis, *Chem. Rev.* **2010**, *110*, 6446-6473.
- [7] X. Liu, Z. Cai, L. Wan, P. Xiao, B. Che, J. Yang, H. Niu, H. Wang, J. Zhu, Y. T. Huang, H. Zhu, S. J. Zelewski, T. Chen, R. L. Z. Hoyer, R. Zhou, *Adv. Mater.* **2024**, *36*, 2305841.
- [8] U. Ali Shah, S. Chen, G. Mohamed Gomaa Khalaf, Z. Jin, H. Song, U. A. Shah, S. Chen, G. M. G Khalaf, Z. Jin, H. Song, *Adv. Funct. Mater.* **2021**, *31*, 2100265.
- [9] R. Kondrotas, C. Chen, J. Tang, *Joule* **2018**, *2*, 857–878.
- [10] K. Li, R. Tang, C. Zhu, T. Chen, *Adv. Sci.* **2023**, *11*, 2304963.
- [11] T. Ben Nasr, H. Maghraoui-Meherzi, H. Ben Abdallah, R. Bennaceur, *Physica B Condens. Matter* **2011**, *406*, 287–292.
- [12] H. Jalali, A. A. Orouji, I. Gharibshahian, *Adv. Theory Simul.* **2023**, *7*, 2300594.
- [13] X. Liu, Z. Cai, L. Wan, P. Xiao, B. Che, J. Yang, *Adv. Mater.* **2024**, *36*, 2305841.
- [14] J. A. Christians, D. T. Leighton, P. V Kamat, *Energy Environ. Sci.* **2014**, *7*, 1148-1158.
- [15] Z. Cai, C.-M. Dai, S. Chen, *Solar RRL* **2019**, *4*, 1900503.
- [16] J. Chen, G. Li, Z. Xu, C. Xu, F. Naveed, B. Liu, Y. Zhang, R. Zhou, C. Chen, M. Wang, J. Xu, L. Li, J. Chen, G. Li, Z. Xu, C. Xu, B. Liu, Y. Zhang, J. Xu, F. Naveed, C. Chen, M. Wang, R. Zhou, L. Li, *Adv. Funct. Mater.* **2024**, *34*, 2313676.

- [17] R. G. Sotelo Marquina, T. G. Sanchez, N. R. Mathews, X. Mathew, *Mater. Res. Bull.* **2017**, *90*, 285–294.
- [18] P. Büttner, F. Scheler, C. Pointer, D. Döhler, M. K. S. Barr, A. Koroleva, D. Pankin, R. Hatada, S. Flege, A. Manshina, E. R. Young, I. Mínguez-Bacho, J. Bachmann, *ACS Appl. Energy Mater.* **2019**, *2*, 8747–8756.
- [19] B. Krishnan, A. Arato, E. Cardenas, T. K. D. Roy, G. A. Castillo, *Appl. Surf. Sci.* **2008**, *254*, 3200–3206.
- [20] P. Abraham, S. Shaji, D. A. Avellaneda, J. A. Aguilar-Martínez, B. Krishnan, *Mater. Sci. Semicond. Process* **2023**, *156*, 107269.
- [21] L. Yao, L. Lin, H. Liu, F. Wu, J. Li, S. Chen, Z. Huang, G. Chen, *J. Mater. Sci. Technol.* **2020**, *58*, 130–137.
- [22] N. Velpula, N. Thota, G. H. Chandra, M. Raghavender, D. A. Reddy, P. V. S. Y., *Physica B Condens. Matter* **2024**, *695*, 416484.
- [23] D. Perednis, L. J. Gauckler, *J. Electroceram.* **2005**, *14*, 103–111.
- [24] S.-N. Park, S.-Y. Kim, S.-J. Lee, S.-J. Sung, K.-J. Yang, J.-K. Kang, D.-H. Kim, *J. Mater. Chem. A* **2019**, *7*, 25900-25907.
- [25] Y. Yin, C. Jiang, Y. Ma, R. Tang, X. Wang, L. Zhang, Z. Li, C. Zhu, T. Chen, Y. W. Yin, C. H. Jiang, Y. Y. Ma, R. F. Tang, X. M. Wang, L. J. Zhang, C. F. Zhu, T. Chen, Z. Q. Li, *Adv. Mater.* **2021**, *33*, 2006689.
- [26] H. Cai, R. Cao, J. Gao, C. Qian, B. Che, R. Tang, C. Zhu, T. Chen, H. Cai, R. Cao, J. Gao, B. Che, R. Tang, C. Zhu, T. Chen, *Adv. Funct. Mater.* **2022**, *32*, 2208243.
- [27] M. Ishaq, X. Li, S. Mehmood, Y. M. Zhong, A. Mansoor, U. A. Shah, S. Chen, Y. Chen, Z. Zheng, G. Liang, *Chem. Eng. J.* **2024**, *501*, 157646.
- [28] T. Fukumoto, T. Moehl, Y. Niwa, M. K. Nazeeruddin, M. Grätzel, L. Etgar, *Adv. Energy Mater.* **2012**, *3*, 29-33.
- [29] C. Pointer, P. Büttner, F. Scheler, D. Döhler, I. Mínguez-Bacho, J. Bachmann, E. R. Young, *J. Phys. Chem. C* **2021**, *125*, 18429–18437.
- [30] L. Wang, W. Lian, B. Liu, H. Lv, Y. Zhang, X. Wu, T. Wang, J. Gong, T. Chen, H. Xu, L. Wang, Y. Zhang, H. Xu, W. Lian, H. Lv, X. Wu, T. Chen, B. Liu, T. Wang, J. Gong, *Adv. Mater.* **2022**, *34*, 2200723.
- [31] R. R. Prabhakar, T. Moehl, S. Siol, J. Suh, S. D. Tilley, *Chem. Mater.* **2020**, *32*, 7247–7253.
- [32] F. Yang, J. Xi, L. Y. Gan, Y. Wang, S. Lu, W. Ma, F. Cai, Y. Zhang, C. Cheng, Y. Zhao, *J Colloid Interface Sci.* **2016**, *464*, 1–9.

- [33] W. Zi, F. Mu, X. Lu, Z. Liu, X. Pang, Z. Yu, Y. Li, Z. Zhao, B. Lei, N. Cheng, Z. Xiao, *Mater. Sci. Semicond. Process* **2023**, *153*, 107185.
- [34] H. Wei, J. Shi, X. Xu, J. Xiao, J. Luo, J. Dong, S. Lv, L. Zhu, H. Wu, D. Li, Y. Luo, Q. Meng, Q. Chen, *Phys. Chem. Chem. Phys.* **2015**, *17*, 4937–4944.
- [35] V. Sharma, A. C. Dakshinamurthy, B. Pandey, S. C. Roy, C. Sudakar, *Nano Express* **2020**, *1*, 030038.
- [36] Y. S. Lee, J. Heo, S. C. Siah, J. P. Mailoa, R. E. Brandt, S. B. Kim, R. G. Gordon, T. Buonassisi, *Energy Environ. Sci.* **2013**, *6*, 2112–2118.
- [37] J. Han, H. Yan, C. Hu, Q. Song, J. Kang, Y. Guo, Z. Liu, J. Han, H. Yan, C. Hu, Q. Song, J. Kang, Y. Guo, Z. Liu, *Small* **2022**, *18*, 2105026.
- [38] P. Büttner, F. Scheler, D. Döhler, M. K. S. Barr, M. Bosch, M. Rey, T. Yokosawa, S. Hinz, J. Maultzsch, E. Spiecker, N. Vogel, I. Mínguez-Bacho, J. Bachmann, *Nano Energy* **2022**, *103*, 107820.
- [39] M. Tutundzic, X. Zhang, S. Lammar, S. Singh, P. Marchezi, T. Merckx, A. Aguirre, E. Moons, T. Aernouts, Y. Kuang, B. Vermang, *Solar RRL* **2023**, *8*, 2300862.
- [40] A. Farag, T. Feeney, I. M. Hossain, F. Schackmar, P. Fassel, K. Küster, R. Bäuerle, M. A. Ruiz-Preciado, M. Hentschel, D. B. Ritzer, A. Diercks, Y. Li, B. A. Nejjand, F. Laufer, R. Singh, U. Starke, U. W. Paetzold, *Adv. Energy Mater.* **2023**, *13*.
- [41] W. Ke, D. Zhao, A. J. Cimaroli, C. R. Grice, P. Qin, Q. Liu, L. Xiong, Y. Yan, G. Fang, *J. Mater. Chem. A* **2015**, *3*, 24163–24168.
- [42] C. Altinkaya, E. Aydin, E. Ugur, F. H. Isikgor, A. S. Subbiah, M. De Bastiani, J. Liu, A. Babayigit, T. G. Allen, F. Laquai, A. Yildiz, S. De Wolf, C. Altinkaya, A. Yildiz, A. Babayigit, *Adv. Mater.* **2021**, *33*, 2005504.
- [43] A. Uddin, H. Yi, *Solar RRL* **2022**, *6*, 2100983.
- [44] K. C. Wang, P. S. Shen, M. H. Li, S. Chen, M. W. Lin, P. Chen, T. F. Guo, *ACS Appl. Mater. Interfaces* **2014**, *6*, 11851–11858.
- [45] R. Betancur, Maymóc, X. Elias, L. T. Vuong, J. Martorell, *Sol. Energy Mater. Sol. Cells* **2011**, *95*, 735–739.
- [46] P. Subramanyam, M. Deepa, S. Santosh Kumar Raavi, H. Misawa, V. Biju and C. Subrahmanyam, *Nanoscale Adv.* **2020**, *2*, 5591.
- [47] H. Wang, X. Song, M. Lv, S. Jin, J. Xu, X. Kong, X. Li, Z. Liu, X. Chang, W. Sun, J. Zheng, X. Li, H. Wang, X. Song, M. Lv, S. Jin, X. Chang, W. Sun, J. Xu, X. Li, X. Kong, Z. Liu, J. Zheng, *Small* **2021**, *18*, 2104293.

- [48] S. Yuan, H. Deng, D. Dong, X. Yang, K. Qiao, C. Hu, H. Song, H. Song, Z. He, J. Tang, *Sol. Energy Mater. Sol. Cells* **2016**, *157*, 887–893.
- [49] N. Fleck, T. D. C. Hobson, C. N. Savory, J. Buckeridge, T. D. Veal, M. R. Correia, D. O. Scanlon, K. Durose, F. J. Ackel, *J. Mater. Chem. A* **2020**, *8*, 8337-8344.
- [50] N. Fleck, T. D. C. Hobson, C. N. Savory, J. Buckeridge, T. D. Veal, M. R. Correia, D. O. Scanlon, K. Durose, F. J. Ackel, *J. Mater. Chem. A* **2020**, *8*, 8337-8344.
- [51] Y. C. Choi, D. U. Lee, J. H. Noh, E. K. Kim, S. Il Seok, *Adv. Funct. Mater* **2014**, *24*, 3587–3592.
- [52] M. Y. Versavel, J. A. Haber, *Thin Solid Films* **2007**, *515*, 7171–7176.
- [53] W. Lian, C. Jiang, Y. Yin, R. Tang, G. Li, L. Zhang, B. Che, T. Chen, *Nat. Commun.* **2021**, *12:1* **2021**, *12*, 1–7.
- [54] L. Grad, F. O. Von Rohr, M. Hengsberger, J. Osterwalder, *Phys. Rev. Mater.* **2022**, *5*, 75401.
- [55] Z. Yang, X. Wang, Y. Chen, Z. Zheng, Z. Chen, W. Xu, W. Liu, Y. (Michael) Yang, J. Zhao, T. Chen, H. Zhu, *Nat. Commun.* **2019**, *10*, 4540.
- [56] A. D. Deangelis, Kingsley, C. Kemp, N. Gaillard, K. S. Kim, *ACS Appl. Mater. Interfaces* **2016**, *8*, 8445-8451.
- [57] J. Zheng, C. Liu, L. Zhang, Y. Chen, F. Bao, J. Liu, H. Zhu, K. Shen, Y. Mai, *Chem. Eng. J.* **2022**, *446*, 136474.